Melting of magnesium oxide to 2 terapascals using double-shock compression

L. E. Crandall,[1,2] D. E. Fratanduono,[3] S. Zhang,[1] D. G. Hicks,[4] T. Suer,[1,5] Z. K. Sprowal,[1,2] M. F. Huff,[1,2] X. Gong,[1,6] B. J. Henderson,[1,2] D. N. Polsin,[1,6] M. Zaghoo,[1] S. X. Hu,[1,6] G. W. Collins,[1,2,6] and J. R. Rygg[1,2,6]

[1]*Laboratory for Laser Energetics, Rochester, New York 14623, USA*
[2]*Department of Physics, University of Rochester, Rochester, New York 14611, USA*
[3]*Lawrence Livermore National Laboratory, Livermore, California 94550-9234, USA*
[4]*Optical Sciences Centre, Swinburne University of Technology, Hawthorn, VIC 3122, Australia*
[5]*Department of Earth and Planetary Sciences, Harvard University, Cambridge, Massachusetts 02138, USA*
[6]*Department of Mechanical Engineering, University of Rochester, Rochester, New York 14611, USA*

(Dated: April 21, 2021)

Magnesium oxide is a major constituent of gaseous and rocky planets. Constraining its melting behavior at extreme conditions is key to understanding planetary interior evolution. Using a double-shock technique, we extended the MgO melt curve to 2 TPa; this is twice the pressure achieved by previous melting experiments on any material. A temperature plateau was observed between 1218 and 1950 GPa in the second shock states due to latent heat. At 1950 GPa, the measured melting temperature is 17,600 K, 17% lower than recent theoretical predictions. The melting curve is steeper than that of $MgSiO_3$, indicating that MgO is unlikely to exist in liquid form in the interior of solar gas giants and extra-solar super-Earths.

Magnesium oxide (MgO, periclase) is an end-member of the (Mg, Fe) O magnesiowüstite mineral, a major constituent of the Earth's lower mantle [1, 2]. It is likely present in the deep interiors of gas giants such as Jupiter and Saturn and in rocky extra-solar planets known as super-Earths [3, 4]. As an abundant component in planets, the physical properties of MgO can influence planetary structure and evolution. The B2 phase (CsCl-type) of MgO is expected to be abundant in the mantles of super-Earths and in the rocky cores of gas giants due to the dissociation of $MgSiO_3$-perovskite [4]. The melting of MgO could therefore be an important driver of thermal and chemical exchange in the mantles and the coremantle boundaries regions of these planets [5, 6]. Recent works have invoked MgO exsolution from the cores of Earth and other large rocky planets as a mechanism capable of powering a planetary magnetic dynamo [7, 8]. Quantifying the melting behavior of MgO to the high pressures and temperatures of planetary interiors is therefore relevant to investigating a number of topical issues in planetary science.

The melt curve of MgO has been studied up to 40 GPa using laser- and resistance-heated multi- and diamond-anvil cells [9–12], and up to 550 GPa on the principal Hugoniot (locus of states attainable with a single shock wave) with decaying shock experiments [13, 14]. Single shock waves can be used to study melting of a material to the pressure at which the principal Hugoniot crosses the melt curve; however, different experimental techniques are necessary to probe melting at higher pressures. For example, the melt curve of SiO_2 has been experimentally probed beyond the principal Hugoniot of common polymorphs fused silica and quartz using single shocks in the high-density polymorph stishovite [18]. MgO has no stable high-density polymorphs; the NaCl-type B1 phase of ambient MgO has been observed to be stable to hundreds of GPa in static-compression experiments [19]. A different experimental technique was required in order to study the high-pressure melting behavior of MgO. While

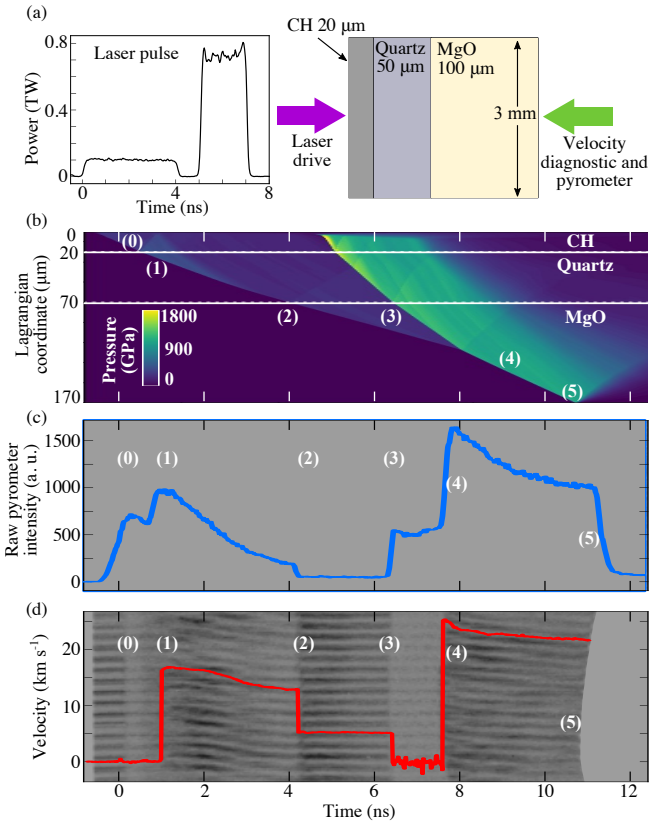

FIG. 1: (a) *Left:* The laser pulse on shot 28954. *Right:* A schematic of the target design. (b) A Lagrangian x–t diagram displaying pressure contours from a hydrodynamic simulation of the laser pulse and target in (a). (c) The raw pyrometer image from shot 28954 with the intensity over-plotted in blue. (d) The raw velocimeter image from shot 28954 with the extracted velocity over-plotted in red. The enumerated events in (b), (c), and (d) are described in the text.

the double-shock tecnique using anvils has been used for decades, the double-shock self-impedance matching technique was first described in Ref. [20] and was used to study off-Hugoniot fluid states of SiO_2 [21]. In this work, we apply the double-shock technique to measure the melt curve of MgO to 2 TPa, the highest pressure any material's melt curve has been studied experimentally.

These experiments were performed on the OMEGA EP Laser System at the Laboratory for Laser Energetics in Rochester, NY [22]. Targets consisted of a 20-μm-thick CH polystyrene ablator, a 50-μm-thick α-quartz pusher, and a 100- or 200-μm-thick single-crystal $< 100 >$ MgO sample. All pieces were laterally 3-mm squares. The target components were held together with 1–3 μm of low-viscosity epoxy. The quartz pusher served to produce steady shocks in the MgO sample and as a temperature/reflectivity reference [23, 24]. Two successive shock waves were launched into the sample with a dual laser pulse through ablation of the CH. A laser pulse from an experiment and a schematic of the target stack are depicted in Fig. 1 (a). The first shock was produced with 400 J in a single laser beam with a 6- or 4-ns flattop pulse (0.067 TW or 0.1 TW); the second shock was produced with a net 1500 to 6400 J in one to three beams with a 2-ns flattop pulse (0.75 to 3.2 TW). Distributed phase plates were used to create a spatially uniform irradiance profile with a 95% encircled energy spot diameter of 1100 μm.

The time-resolved diagnostics included an SOP (streaked optical pyrometer) [25] and a dual-channel line-imaging VISAR (velocity interferometer system for any reflector) [26]. The SOP measured self-emission throughout the experiment in the range of 590 to 750 nm with a peak system response at 609 nm. The VISAR measured the velocity of reflecting interfaces or shock fronts with a 532-nm probe beam; the amplitude of the VISAR signal was used to determine reflectivity at 532 nm. Both VISAR and SOP have a field of view of 1-mm. Figure 1 (b) is a Lagrangian x–t diagram with pressure contours from a LILAC hydrodynamic simulation of an experiment [27]. Figure 1 (c) is an SOP image from an experiment with the raw intensity versus time overplotted in blue; Fig. 1 (d) is the corresponding streaked VISAR image for that experiment with the extracted velocity versus time profile throughout the experiment over-plotted in red.

A sequence of events was observed in a single experiment, as enumerated in Figs. 1 (b)–(d). In region (0), the first laser pulse is launched, inducing the first shock in CH. A drop in the reflectivity is observed in VISAR, and emission from the CH ablator is measured with SOP. In region (1), the first shock enters the quartz pusher; shock velocity and emission from the shock front in quartz are measured.

In region (2), the first shock has been transmitted into the MgO sample. When the shock passes from the quartz into the higher-impedance MgO, a reshock is launched back into the quartz [28]. The emission from the reshocked quartz is absorbed by the shocked glue layer between the quartz and the MgO. The emission of the first shock in MgO is too low to observe with SOP; low signal of approximatly 50 analog-to-digital units measured with SOP in region (2) is attributed to the shocked glue [29]. The quartz–MgO interface velocity is measured behind the optically transparent first shock front with VISAR; the refractive index correction and possible effects of first-shock absorption are discussed in the Supplemental Materials [29]. The first shocks in the present work range from 157 to 253 GPa. The B1 phase of MgO is experimentally shown to be stable to at least 360 GPa on the principal Hugoniot [13], which is consistent with recent theory [30]. Additionally, above 97 GPa, the elastic precursor of MgO is overdriven [31]. Therefore, the first shocks in this work exhibit no multi-wave structure.

Because the first shock in the MgO is temporally steady, the measured quartz–MgO interface velocity is equal to the particle velocity (U_{p1}) of the MgO behind the first shock front. The first shock lies on the principal Hugoniot. The pressure, density, and temperature of the B1-phase principal Hugoniot have been measured previously [31–36]. The first shock velocity was determined from U_{p1} with the optimized linear shock velocity versus particle velocity fit in Ref. [36], and the pressure, density, and internal energy of the first shock were inferred from the Rankine–Hugoniot conditions for conservation of mass, momentum, and energy across a shock front [37]. The first shock temperature was taken from the measured first shock pressure and the density functional theory pressure-temperature Hugoniot in Ref. [36], which shows excellent agreement with existing MgO B1 Hugoniot temperature data [32].

In region (3), the second shock has entered the MgO sample. Transit time measurements were used to determine the average velocity of the second shock wave because the second shock was not reflective enough to be directly measured with VISAR, as seen in Fig. 1 (d), region (3). The second shock pressure, density, and internal energy are obtained by self-impedance matching at the point of shock coalescence [20, 29]. The in-flight emission from the second shock in MgO is measured with SOP through the transparent first shock [Fig. 1 (c), region (3)]. A brightness temperature was inferred from this measured emission by referencing to the temperature in the quartz, which has been studied previously [23, 24]. The brightness temperature was corrected for the reflectivity of the second shock in a grey-body model. The reflectivity of the coalesced shock served as an upper bound for the reflectivity of the second shocks [29]; this is reflected in the error bars of the temperature.

In region (4), the two shocks coalesce into a single decaying shock moving through ambient MgO. This coalesced shock wave resides on the principal Hugoniot in the liquid regime of MgO, which has been previously measured [13, 14, 36, 38, 39]. The velocity of the co-

alesced shock wave was measured with VISAR and corrected for the refractive index of ambient MgO at 532 nm, n = 1.743 [40]. The corresponding particle velocity was determined from the linear shock velocity versus particle velocity fit in Ref. [38]. The pressure, density, and internal energy are inferred from the Rankine–Hugoniot conservation relations [37]. The reflectivity of the coalesced shock is measured with VISAR and referenced to the known quartz Hugoniot reflectivity [23, 24, 29]. The temperature of the coalesced shock is determined from the measured SOP emission and VISAR reflectivity, and referenced to the known quartz Hugoniot temperature [23, 24, 29]. At event (5), the coalesced shock wave breaks out of the MgO into vacuum.

Coalesced shock pressures in the present work range from 1080 to 1989 GPa; corresponding second shock pressures determined from self-impedance matching are 7 to 11% higher than the coalesced shocks, ranging from 1170 to 2109 GPa. An uncertainty of 4–6% in the second shock velocity resulting from transit time measurements, propagated with a 100,000 trial Monte Carlo method, led to uncertainties in the second shock density reaching 14% but only 5% in pressure; this comes directly from the Rankine–Hugoniot conservation relations for mass and momentum. The coalesced shock reflectivity and temperature measured in this work [29] are consistent with previous results [13, 14, 38], lending confidence to this analysis.

The measured first (black cirlces) and second (red cirlces) shock pressure and temperature results are plotted in Fig. 2. At a phase boundary, a material's Hugoniot is often marked by a plateau or reversal in temperature with increasing pressure as thermal energy contributes to a phase transition [42, 43]. This behavior has been observed in shock experiments on diamond [44], SiO_2 [24], and the principal Hugoniot of MgO [13, 14]. A temperature increase in the second shock results of only 3,000 K is observed from 1.2 to 2 TPa; above this pressure, temperature rises rapidly. The three central second shock data points are interpreted to lie on the melt curve of MgO because they demonstrate a lack of heating across a large increase in shock pressure, which is attributed to the latent heat of MgO melting. Liquid MgO at 2109 GPa and 26.2 kK must have a reflectivity of less than a few percent, because a reflecting second shock front was not measured, indicating that MgO may melt into an insulating state. These experiments did not determine the structure of solid MgO, and no structural data exist at these pressures. It is assumed that the MgO melts from B2 in these experiments because no other solid phases are predicted above the B1-B2 transition.

As demonstrated in Fig. 2, there is discrepancy in where the principal Hugoniot of MgO crosses the B1-B2 transition and the melt curve. A large temperature reversal at 470 (40) GPa observed in decaying shock experiments in Ref. [14] was attributed to MgO melting (blue circle). In nearly identical decaying shock experiments in Ref. [13], the observed temperature reversal at 440 (80) GPa was attributed to the B1-B2 transition (light blue x), while a small slope change in the Hugoniot at 650 (50) GPa was attributed to melting (green cirlce). Density functional theory and quantum Monte Carlo theoretical methods (red dotted-dashed curves) predict a steep melting curve [36] consistent with the interpretation of melt from Ref. [13], but the location of the B1-B2 transition in Ref. [36] is not consistent with that from Ref. [13]. First principles molecular dynamics studies from Ref. [15] (pink dotted-dashed curve) predict a gentle melt slope consistent with the melting interpretation from Ref. [14]. Recent density functional molecular dynamic calculations predict a melting curve that sits in between the interpretations of the experiments from both Ref. [14] and [13]. Furthermore, x-ray diffraction experiments on ramp compressed MgO measure the B1-B2 phase transition at 600 GPa [41] (gold x); this is higher pressure than predicted by any models for the B1-B2 transition.

To capture the shape of the high pressure melt curve, we performed a fit to our data and lower pressure melting

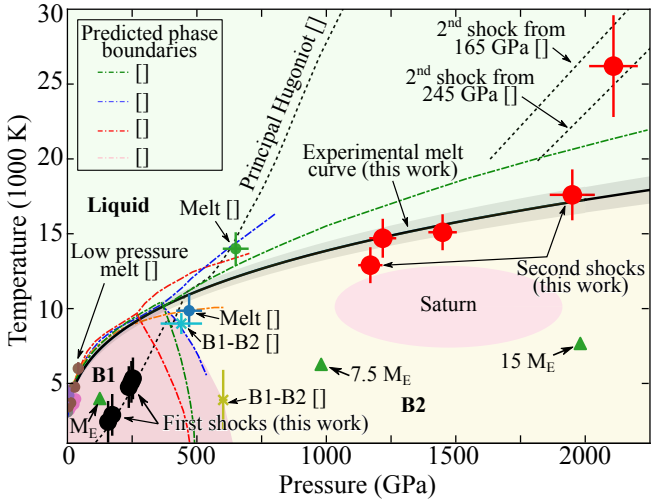

FIG. 2: The phase diagram of MgO. Black circles represent the first shock B1 states in the present work; pressure is measured, and temperature is known from previous work [36]. Red cirlces are the second shock states; both pressure and temperature are measured.The three central second shock states are interpreted to be on the melting curve of MgO due to a lack of heating across a large increase in pressure. Melting data from previous experiments are plotted with small circles cirlces [9–14], and B1-B2 transition data are plotted with x's [13, 41]. Dotted-dashed curves are previously predicted phase boundaries [13, 15, 30, 36]. Dashed lines are predictions for the principal Hugoniot and secondary Hugoniots from 165 and 245 GPa first shocks [30, 46–48]. The core–mantle boundary conditions are plotted for Saturn [16] and 1–, 7.5–, and 15–Earth-mass (M_E) super-Earths [17]. The solid black curve is Simon-Glatzel fit (Eq. 1) to the melting data in this work and the melting data from Refs. [10, 12], with grey shading representing the uncertainty in the fit parameters.

data from Refs. [10, 12] with a Simon–Glatzel equation of the form:

$$T_m[K] = 3098\left(\frac{P_m[GPa]}{a} + 1\right)^{1/b} \quad (1)$$

where T_m and P_m are the temperature and pressure of the melt curve, and 3098 K is the melting temperature of MgO at atmospheric pressure [10]. This emperical relation has been used to describe the melting behavior of other oxides including SiO_2 [18] and $MgSiO_3$ [45]. The best fit parameters are given by $a = 9.15 \pm 2.23$ GPa and $b = 3.14 \pm 0.19$ with a covariance of -0.39, determined from a non-linear least squares analysis. The decaying shock melting data [13, 14] were not included in this fit because of the disagreement in interpretation of experiments as discussed above. The fit in Eq. 1 does not allow for a change in slope at the B1-B2-liquid triple point; the pressure and temperautre of the triple point have not been measured, and theoretical approaches disagree on its location. Fits based on different interpretations of the melting data in Refs. [13, 14], and on different predicted locations of the triple point, are discussed in the Supplemental Materials [29].

The melt curve in Eq. 1 is plotted in Fig. 2 (solid black) and shows strong agreement with recent density functional theory [30] (dotted-dashed green curve) up to 650 GPa before the curves diverge. Reference [30] overestimates the measured melting temperature at 1950 GPa by 17%. The discrepancy between experiment and theory on the melt curve could have profound origins, due to the complex elastic and plastic responses of MgO during the shock/re-shock and phase transformation processes, which have complicated the measurements but not been taken into account in the first principles calculations. This calls for larger-scale non-equilibrium simulations and crystallographic diagnostics to better understand problems as such. A previously published melting curve of MgO [18] based on extrapolation of data from Refs. [10, 11, 13] overestimates the melting temperature at 1950 GPa by 27%.

The highest-pressure second shock equation-of-state point in this work is in the liquid regime of the 173 GPa secondary Hugoniot of MgO and shows general agreement with First-Principles Equation of State simulations of secondary Hugoniots from similar initial shock conditions [46–48]; the slope of the secondary Hugoniot defined by the two highest-pressure second shock points in this work does appear steeper than theoretical predictions, but is consistent with theory given the error bars. The low-pressure second-shock data in this work demonstrate that the double-shock technique is a valuable method for probing the behavior of MgO in the solid phase at the temperatures and pressures directly relevant to the core–mantle boundary of gas giants similar in size and composition to Saturn [16] and super-Earths in the 7.5 to 15–Earth-mass range [17].

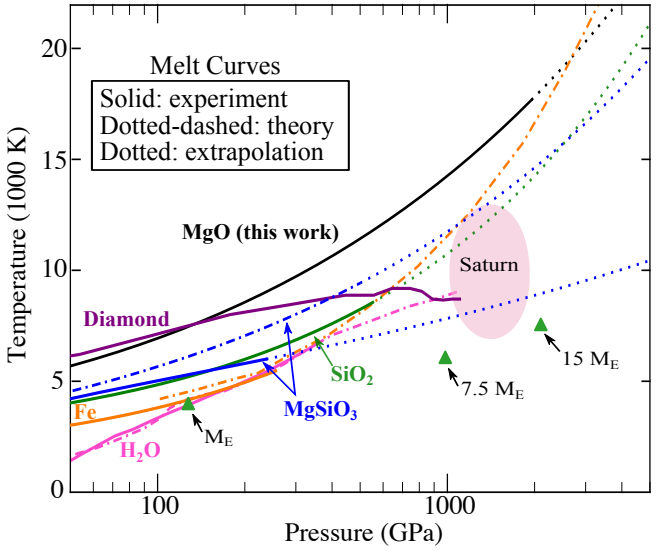

FIG. 3: A comparison of melt curves of planetary materials. Diamond: experiment (solid purple [44]). SiO_2: experiment and extrapolation (solid and dotted green [18]). $MgSiO_3$: experiment (solid blue [45]), theory (dotted-dashed blue [49]), and extrapolations (dotted blue). Fe: experiment (solid orange [50]) and theory (dotted-dashed orange [51]). H_2O superionic melt: experiment (solid pink [52]) and theory (dotted-dashed pink [53]). The present experimental work on MgO (solid black, extrapolated with dotted black) represents the highest pressure to which a melt curve has ever been measured. The core–mantle boundary conditions are plotted for Saturn [16] and 1–, 7.5–, and 15–Earth-mass (M_E) super-Earths [17].

The melt curve of MgO measured in this work is presented in Fig. 3 along with those of other abundant planetary materials including SiO_2 [18], $MgSiO_3$ [45, 49], diamond [44], Fe [50, 51], and H_2O [52, 53]. MgO remains solid at a higher temperature than all other planetary materials up to 2 TPa; above this pressure, the MgO melt curve may cross that of iron. MgO has a steeper melt curve than $MgSiO_3$ above 150 GPa, suggesting that pressure-induced dissociation of liquid $MgSiO_3$ at 10,000 K and 1 TPa [4] inside super-Earths or gas giants may result in a solid MgO layer. If MgO is present in multicomponent systems (e.g., MgO-FeO-SiO2), eutectic melting could lower the melting temperature [55]. However, the rocky core of Saturn most likely supports solid MgO and SiO_2. Because solid B2-phase MgO is only weakly soluble in fluid hydrogen, the protocore of Saturn likely remained stable throughout its evolution [54].

Dissolution of Mg into the Fe core of super-Earths during planetary formation could have important consequence for planetary structure and interior processes. One possible scenario includes MgO exsolution from the core, which could potentially provide enough energy to power a geodynamo and generate a planetary magnetic field [7, 8]. Depending on the quantity of material exsolved, a layer of MgO could precipitate at the planet's core–mantle boundary. Metallic behavior of MgO [13] at

this depth could strongly influence further core-mantle interactions and magnetic field generation. Alternatively, if metallic MgO were to remain dissolved in an Fe core, a layered core structure could result [56]. Further measurements of melting behaviors of other major planet forming oxides are necessary for further investigating these deep planetary processes which could be important in the search for Earth-like planets.

In summary, the present work utilizes a double-shock technique to probe the melt curve of MgO to unprecedented pressures. A plateau in temperature from 1.2 to 2 TPa suggests a large solid/liquid coexistence region similar to that seen in decaying single-shock experiments on diamond [44]. MgO remains solid at TPa pressures to higher temperatures than all other planetary materials and is therefore unlikely to exist a liquid state in the cores or mantles of known giant planets. This work is a new benchmark for measuring the properties of planetary materials at extreme pressures and temperatures. The results will be useful for investigating planetary structure models and the processes in deep planetary interiors for a range of planet sizes including gas giants and super-Earths. Additionally, the technique presented in this work will lead to new advances in probing phase transitions of transparent materials up to TPa pressures and will significantly advance the scientific community's understanding of the behavior of warm dense matter at extreme conditions.

Acknowledgments

This material is based upon work supported by the Department of Energy National Nuclear Security Administration under Award Number DE-NA0003856, the University of Rochester, the New York State Energy Research and Development Authority, the NSF Physics Frontier Center award PHY-2020249, and the Australian Research Council grant FT140101104. Lawrence Livermore National Laboratory is operated by Lawrence Livermore National Security, LLC, for the U.S. Department of Energy, National Nuclear Security Administration under Contract DE-AC52-07NA27344. The Lawrence Livermore National Laboratory AnalyzeVISAR code written by J. H. Eggert, R. S. McWilliams, D. E. Fratanduono, and M. Millot was used to process part of the VISAR and SOP data. The authors thank M. Ginnane of the University of Rochester Mechanical Engineering Department and the Laboratory for Laser Energetics for her work on the calibration of the SOP system on OMEGA EP.

[1] W. F. McDonough and S.-s. Sun, Chem. Geol. **120**, 223 (1995).
[2] J.-Fu. Lin, D. L. Heinz, H.-k. Mao, R. J. Hemley, J. M. Devine, J. Li, and G. Shen, Proc. Natl. Acad. Sci. **100**, 4405 (2003).
[3] S. Seager, M. Kuchner, C. A. Hier-Majumder, and B. Militzer, Astrophys. J. **669**, 1279 (2007).
[4] K. Umemoto, R. M. Wentzcovitch, and P. B. Allen, Science **311**, 983 (2006)
[5] L. Strixude, Phil. Trans. R. Soc. A **372**, 20130076 (2014).
[6] W. B. Tonks and H. J. Melosh, J. Geophys. Res. **98**, 5319 (1993).
[7] J. Badro, J. Siebert, and F. Nimmo, Nature **536**, 326 (2016).
[8] J. G. O'Rourke and D. J. Stevenson, Nature **529**, 387 (2016).
[9] A. Zerr and R. Boehler, Nature **371**, 506 (1994).
[10] L. S. Dubrovinsky and S. K. Saxena, Phys. Chem. Miner. **24**, 547 (1997).
[11] L. Zhang and Y. Fei, Geophys. Res. Lett. **35** (2008).
[12] Z. Du and K. K. M. Lee, Geophys. Res. Lett. **41**, 8061 (2014).
[13] R. S. McWilliams, D. K. Spaulding, J. H. Eggert, P. M. Celliers, D. G. Hicks, R. F. Smith, G. W. Collins, and R. Jeanloz, Science **338**, 1330 (2012).
[14] R. M. Bolis, G. Morard, T. Vinci, A. Ravasio, E. Bambrink, M. Guarguaglini, M. Koenig, R. Musella, F. Remus, J. Bouchet et al., Geophys. Res. Lett. **43**, 9475 (2016).
[15]
[16] F. Gonzalez-Cataldo, H. F. Wilson, and B. Militzer, Astrophys. J. **787**, 79 (2014).
[17] F. W. Wagner, N. Tosi, F. Sohl, H. Rauer, and T. Spohn, Astron. Astrophys. **541**, A103 (2012).
[18] M. Millot, N. Dubrovinskaia, A. ernok, S. Blaha, L. Dubrovinsky, D. G. Braun, P. M. Celliers, G. W. Collins, J. H. Eggert, and R. Jeanloz, Science **347**, 418 (2015).
[19] T. S. Duffy, R. J. Hemley, and H. K. Mao, Phys. Rev. Lett. **74**, 1371 (1995).
[20] M. Guarguaglini, J.-.A. Hernandez, A. Benuzzi-Mounaix, R. Bolis, E. Brambrink, T. Vinci, and A. Ravasio, Phys. Plasmas **26**, 042704 (2019).
[21] M. Guarguaglini, F. Soubiran, J.-A. Hernandez, A. Benuzzi-Mounaix, R. Bolis, E. Brambrink, T. Vinci, and A. Ravasio, Nat. Comm. **12**, 840 (2021).
[22] D. D. Meyerhofer, J. Bromage, C. Dorrer, J. H. Kelly, B. E. Kruschwitz, S. J. Loucks, R. L. McCrory, S. F. B. Morse, J. F. Myatt, P. M. Nilson et al., J. Phys.: Conf. Ser. **244**, 032010 (2010).
[23] S. Brygoo, M. Millot, P. Loubeyre, A. E. Lazicki,

S. Hamel, T. Qi, P. M. Celliers, F. Coppari, J. H. Eggert, D. E. Fratanduono et al., J. Appl. Phys. **118**, 195901 (2015).
[24] D. G. Hicks, T. R. Boehly, J. H. Eggert, J. E. Miller, P. M. Celliers, and G. W. Collins, Phys. Rev. Lett. **97**, 025502 (2006).
[25] J. E. Miller, T. R. Boehly, A. Melchior, D. D. Meyerhofer, P. M. Celliers, J. H. Eggert, D. G. Hicks, C. M. Sorce, J. A. Oertel, and P. M. Emmel, Rev. Sci. Instrum. **78**, 034903 (2007).
[26] P. M. Celliers, D. K. Bradley, G. W. Collins, D. G. Hicks, T. R. Boehly, and W. J. Armstrong, Rev. Sci. Instrum. **75**, 4916 (2004).
[27] J. Delettrez, R. Epstein, M. C. Richardson, P. A. Jaanimagi and B. L. Henke, Phys. Rev. A **36**, 3926 (1987).
[28] R. G. McQueen, S. P. Marsh, J. W. Taylor, J. N. Fritz, and W. J. Carter, in *High-Velocity Impact Phenomena*, edited by R. Kinslow (Academic Press, New York, 1970).
[29] See the Supplemental Material at [link]
[30] F. Soubiran and B. Militzer, Phys. Rev. Lett. **125**, 175701 (2020).
[31] D. E. Fratanduono, J. H. Eggert, M. C. Akin, R. Chau, and N. C. Holmes, J. Appl. Phys. **114**, 043518 (2013).
[32] B. Svendsen and T. J. Ahrens, Geophys. J. Int. **91**, 667 (1987).
[33] M. S. Vassiliou and T. J. Ahrens, Geophys. Res. Lett. **8**, 729 (1981).
[34] T. S. Duffy and T. J. Ahrens. J. Geophys. Res. Solid Earth **100**, 529 (1995).
[35] L. Zhang, Z. Gong, and Y. Fei, J. of Phys. and Chem. Solids **69**, 2344 (2008).
[36] S. Root, L. Shulenburger, R. W. Lemke, D. H. Dolan, T. R. Mattsson, and M. P. Desjarlais, Phys. Rev. Lett. **115**, 198501 (2015).
[37] Ya. B. Zeldovich and Yu. P. Razer, in *Physics of Shock Waves and High-Temperature Hydrodynamic Phenomena*, edited by W. D. Hayes and R. F. Probstein (Dover Publications, Mineola, NY, 2002).
[38] C. A. McCoy, M. C. Marshall, D. N. Polsin, D. E. Fratanduono, P. M. Celliers, D. D. Meyerhofer, and T. R. Boehly, Phys. Rev. B **100**, 014106 (2019).
[39] K. Miyanishi, Y. Tange, N. Ozaki, T. Kimura, T. Sano, Y. Sakawa, T. Tsuchiya, and R. Kodama, Phys. Rev. E **92**, 023103 (2015).
[40] R. E. Stephens and I. H. Malitson, J. Res. Natl. Bur. Stand. **49**, 249 (1952).
[41] F. Coppari, R. F. Smith, J. H. Eggert, J. Wang, J. R. Rygg, A. Lazicki, J. A. Hawreliak, G. W. Collins, and T. S. Duffy, Nat. Geosci. **6**, 926 (2013).
[42] S. B. Kormer, Sov. Phys.-Usp. **11**, 229 (1968).
[43] G. Lyzenga, T. J. Ahrens, and A. C. Mitchell, J. Geophys. Res. **88**, 2431 (1983).
[44] J. H. Eggert, D. G. Hicks, P. M. Celliers, D. K. Bradley, R. S. McWilliams, R. Jeanloz, J. E. Miller, T. R. Boehly, and G. W. Collins, Nat. Phys. **6**, 40 (2010).
[45] D. E. Fratanduono, M. Millot, R. G. Kraus, D. K. Spaulding, G. W. Collins, P. M. Celliers, and J. H. Eggert, Phys. Rev. B **97**, 214105 (2018).
[46] F. Soubiran, F. Gonzalez-Cataldo, K. P. Driver, S. Zhang, and B. Militzer, J. Chem. Phys. **151**, 214104 (2019).
[47] B. Militzer, F. Gonzalez-Cataldo, S. Zhang, K. P. Driver, and F. Soubiran, Phys. Rev. E **103**, 013203 (2021).
[48] The principal and the second-shock Hugoniots at 20,000 K or higher are calculated by using the first-principles equation of state (FPEOS) database published in Refs. [46, 47] for MgO. The initial conditions for the second shocks are estimated following the approach of S. Zhang, R. Paul, M. A. Morales, F. Malone, and S. X. Hu, in preparation. See the supplemental material for details.
[49] Y. Fei, C. T. Seagle, J. P. Townsend, C. A. McCoy, A. Boujibar, P. Driscoll, L. Shulenburger, and M. D. Furnish, *Nat. Comm.* **12**, 876 (2021).
[50] J. Li, Q. Wu, J. Li, T. Xue, Y. Tan, X. Zhou, Y. Zhang, Z. Xiong, Z. Gao, and T. Sekine, Geophys. Res. Lett. **47**, e2020GL087758 (2020).
[51] D. C. Swift, T. Lockard, R. F. Smith, C. J. Wu, and L. X. Benedict, Phys. Rev. Research **2**, 023034 (2020).
[52] M. Millot, S. Hamel, J. R. Rygg, P. M. Celliers, G. W. Collins, F. Coppari, D. E. Fratanduono, R. Jeanloz, D. C. Swift, and J. H. Eggert, Nat. Phys. **14**, 297 (2018).
[53] R. Redmer, T. R. Mattsson, N. Nettlemann, and M. French, Icarus **211**, 798 (2011).
[54] H. F. Wilson and B. Militzer, Phys. Rev. Lett. **108**, 111101 (2012).
[55]
[56] R. Musella, S. Mazavet, and F. Guyot, Phys. Rev. B **99**, 064110 (2019).